

Journal Pre-proof

Using Ground Penetrating Radar and attribute analysis for identifying depositional units in a fluvial-aeolian interaction environment: The Guandacol Valley, northwest Argentina

Peter Zabala Medina, Carlos Limarino, Néstor Bonomo, Salomé Salvó Bernárdez, Ana Osella

PII: S0895-9811(19)30386-4

DOI: <https://doi.org/10.1016/j.jsames.2019.102467>

Reference: SAMES 102467

To appear in: *Journal of South American Earth Sciences*

Received Date: 30 July 2019

Revised Date: 12 December 2019

Accepted Date: 12 December 2019

Please cite this article as: Zabala Medina, P., Limarino, C., Bonomo, Né., Salvó Bernárdez, Salomé., Osella, A., Using Ground Penetrating Radar and attribute analysis for identifying depositional units in a fluvial-aeolian interaction environment: The Guandacol Valley, northwest Argentina, *Journal of South American Earth Sciences* (2020), doi: <https://doi.org/10.1016/j.jsames.2019.102467>.

This is a PDF file of an article that has undergone enhancements after acceptance, such as the addition of a cover page and metadata, and formatting for readability, but it is not yet the definitive version of record. This version will undergo additional copyediting, typesetting and review before it is published in its final form, but we are providing this version to give early visibility of the article. Please note that, during the production process, errors may be discovered which could affect the content, and all legal disclaimers that apply to the journal pertain.

© 2019 Published by Elsevier Ltd.



CRediT author statement

Peter Zabala Medina: GPR data acquisition and analysis, attribute methodology and software, visualization, **Carlos Limarino:** Conceptualization, writing, review; **Néstor Bonomo:** conceptualization, GPR data acquisition and analysis, attribute methodology and software, formal analysis; **Salomé Salvó Bernárdez:** data curation, visualization; **Ana Osella:** conceptualization, geophysical data acquisition and interpretation, funding.

**Using Ground Penetrating Radar and Attribute Analysis for identifying
depositional units in a fluvial-aeolian interaction environment: the
Guandacol Valley, northwest Argentina**

Peter Zabala Medina^a, Carlos Limarino^b; Néstor Bonomo^a; Salomé Salvó
Bernárdez^b; Ana Osella^a

^a IFIBA, CONICET - Departamento de Física, Universidad de Buenos Aires,
1428 Ciudad Universitaria, Buenos Aires, Argentina.

^b IGEBA - Departamento de Geología, Universidad de Buenos Aires. 1428
Ciudad Universitaria, Buenos Aires, Argentina.

Emails of the authors:

pzabalamedina@gmail.com

oscarlimarino@gmail.com

bonomo@df.uba.ar

osella@df.uba.ar

salomecandelasb@gmail.com

Corresponding author: Néstor Bonomo. Fax: 54-11-5285-7570. Email:

bonomo@df.uba.ar

Abstract

This paper deals with the application of the Ground Penetrating Radar (GPR) method and the analysis of attributes of the GPR data to characterize and interpret a fluvial-aeolian interaction field located in the Guandacol Valley, northwest Argentina. Several profiles over dunes, interdunes, aeolian mesoforms, and fluvial channels have been acquired. Each data section is analyzed by using standard images of the amplitude of the electric field, as well as representations of different attributes of the reflections such as contrast, dip, curvature, parallelism, and RMS frequency. The analysis of attributes improves the interpretation of the subsurface, by quantifying and making evident properties of the reflection patterns that characterize the sedimentary units. The information obtained using the GPR profiles allows defining seven radar packages, which are useful for reconstructing the internal structure of the fluvial-aeolian succession. Packages 1, 2 and 3 illustrate the stratification of different types of low-sinuosity and high-sinuosity aeolian dunes, as well as aeolian mesoforms. Package 4 corresponds to horizontal or low-angle inclined reflectors obtained in both sandy interdunes and upper parts of several aeolian dunes. A muddy bed that covers most of the area (package 5) probably indicates a period of climate amelioration linked to a high level of the water table. The fluvial component of the fluvial-aeolian succession exhibits two different packages; package 6 represents the infill of partially incised fluvial channels with frequent incisions (concave-up bounding surfaces) and bars (convex-up surfaces). Package 7 is composed of the stacking of parallel to subparallel horizontal reflectors, without concave-up surfaces that indicate deep channels. Finally, we propose a conceptual model that relates the principal

47 radar packages with the temporal evolution of the fluvial-aeolian interaction field
48 of Guandacol Valley.

49

50

51 *Keywords:* Aeolian-fluvial interactions; Depositional architecture; GPR; Radar
52 surface; Data attribute

53

Journal Pre-proof

1. Introduction

During the last ten years, interest in aeolian-fluvial interaction deposits has grown noticeably, because this type of accumulations is relatively frequent in semiarid and arid regions across the entire planet (Bullard and Livingstone, 2002; Veiga et al. 2002; Bullard et al., 2003; Tripaldi and Limarino, 2008; Bongiolo and Scherer, 2010; Al-Masrahy and Mountney, 2015; Liu and Coulthard, 2017). Aeolian-fluvial environments have been studied from different points of view and with different objectives, including geomorphological and sedimentological characterizations (Bullard and Livingstone, 2002; Bullard et al., 2003; Tripaldi and Limarino, 2008; Basilici and Dal'Bó, 2014; Al-Masrahy and Mountney, 2015; Liu and Coulthard, 2015; Mehl et al., 2018), paleoclimatic significance (Spalletti and Veiga, 2007; Roskin et al., 2011), depositional processes (Tripaldi and Limarino 2005; Spalletti et al., 2010; Liu and Coulthard, 2017) and importance as reservoir in the hydrocarbon industry (Herries, 1993; Meadows and Beach, 1993; Iriondo, 1997; Bongiolo and Scherer, 2010).

Beyond the different focus of these studies, aeolian-fluvial environments are considerably complex, since not only fluvial and aeolian processes interplay in the transport and deposition of sediments, but also the erosion in fluvial channels and deflation in aeolian dunes condition the geometry of the resulting deposits. Erosion and deflation form different kinds of bounding surfaces, which differ in geometry, lateral extension, and genetic significance. The nature and importance of these surfaces have been frequently overlooked in the sedimentological studies of the aeolian-fluvial interaction environments. This is

a logical consequence of the finite capacity of the surface survey-methods to recognize and map bounding surfaces of present-day environments.

The ground-penetrating radar (GPR) method is a useful prospecting tool that allows reconstructing the internal structure of the dunes and identify the presence of different types of bounding surfaces. The reflection mode with constant-offset antennae configuration has been the experimental setup most employed for these purposes, because it usually provides good resolution of the reflectors and allows studying large portions of ground in short times. As examples of GPR studies performed in fluvial-aeolian interaction environments, Holland et al. (2006) identified several paleosol reflectors in the northwest Simpson Desert of Australia, which allowed separating different groups of dunes, whereas Bristow et al. (2007) proposed to use GPR in combination with Thermoluminescence studies for reconstructing the stratigraphy of dunes in the center of Australia. Examples of the application of GPR to study aeolian environments are Pedersen and Clemmensen (2005), Girardi and Davis (2010) and Roskin et al. (2013).

The extraction of attributes of the GPR data is used to obtain information that complements and facilitates the interpretation of the traditional amplitude vs. two-way travel time and position sections. Most of the attributes utilized in the GPR area, as reflection inclination, coherence and energy, have their origin in the seismic area (Chopra and Marfurt, 2007; Kumar and Sain, 2018; Wang et al., 2018) and can be applied indistinctly, or with little modifications, to both types of data due to the similarities between the respective waveforms and methodologies. However, the performance and utility of the attributes are

different when applied to GPR and seismic data, since the respective reflection patterns normally have different geometrical and amplitude characteristics (Moysey et al., 2006; Chopra and Marfurt, 2007; McClymont et al., 2008). Then, attributes should be evaluated in both areas independently.

Different types of attributes of the GPR data have been applied to investigate sedimentary deposits. For example, instantaneous attributes, as trace envelope, phase and frequency are valuable for interpreting and discriminating sedimentary units (Moysey et al., 2006; Geerdes and Young, 2007; Ercoli et al., 2015; Nobes et al., 2016; Fu et al., 2018). Texture-based attributes of the images, including energy, contrast, and homogeneity show good capacity for discrimination of radar facies (Moysey et al., 2006; McClymont et al., 2008; Ercoli et al., 2015; Zhao et al., 2018). On the other hand, attributes based on reflection-coherence calculations, as similarity, dip and azimuth have shown useful for characterizing the boundaries of sedimentary units and their internal structure (McClymont et al., 2008; Forte et al., 2012; Andrade dos Reis Jr. et al., 2014; Brandes et al., 2018). However, beyond these works, the use of attributes is relatively uncommon in GPR. For instance, attributes such as the RMS frequency, curvature, and parallelism, though quite frequent in seismic analysis, it has not been almost used in GPR.

In this work, we apply the GPR reflection method and the analysis of attributes of the GPR data sections to recognize, characterize and interpret depositional units and bounding surfaces in the aeolian-fluvial interaction system of the Guandacol Valley (Fig. 1). In this area, Tripaldi and Limarino (2008) studied the interaction between aeolian and fluvial processes by dividing

the investigated areas into areas dominated by fluvial (channels) and aeolian (interchannel) geoforms. In this research, we perform a GPR prospecting of both types of areas, as well as of the closely associated low relief muddy plains, previously identified as muddy sheets in the interchannel areas (Tripaldi and Limarino, 2008). We illustrate the usefulness of calculating different attributes of the GPR data to investigate these deposits, in particular, reflection contrast, RMS frequency, apparent dip, curvature, and parallelism, in addition to the analysis of standard amplitude sections. The information derived from the GPR analysis is used to characterize the fluvial-aeolian interaction system, recognizing different types of aeolian accumulations and the characteristics of the fluvial channels. Finally, we propose a model of the probable temporal evolution of this type of mixed environment.

2. Site description

The fluvial-aeolian interaction deposits analyzed in this paper occur in the Guandacol Valley (1070 meters above sea level), in a fluvial depression located at the foot of the Andean Precordillera, in the north of La Rioja Province (northwestern Argentina, Fig. 1). This valley results from the coalescence of two fluvial systems, which correspond to the Guandacol River (to the west) and La Troya River (to the north), respectively. The area receives only occasional ephemeral floods through a complex network of low-sinuosity channels, which transport gravels and sands mainly during the summer and exceptionally in the spring. During the rest of the year, aeolian sedimentation prevails, either due to the reworking of the fluvial sands or by the wind supply from the south.

The climate of the area is arid to semiarid (Group BWk in the Köppen-Geiger climate classification), with average precipitation of 116 mm, average temperature of 16.5°C and maximum temperature of 32°C in summer.

The area shows two opposite wind patterns, the more persistent flow from the southeast that transport sand from the neighboring dune field of Médanos Grandes (San Juan province) toward the northwest. The second pattern, known as "Troyano" or "Zonda" winds, is more intense and flow from the Andean Cordillera towards the southeast. Beyond the present-day distribution, it is necessary to consider that, during the late Pleistocene and early Holocene, wind patterns suffered important changes. Indeed, Tripaldi (2002) pointed out dramatic changes in wind directions during the construction of the fluvial-aeolian interaction field.

Tripaldi and Limarino (2008) were the first in pointing out the presence of fluvial-aeolian interaction deposits in the valley, dividing these deposits in those placed in channel and interchannel areas. The channel areas comprise different types of bars, streams covered by a veneer of mud, and residual accumulations of boulders and coarse-grained gravels (Fig. 2A). Although aeolian sediments appear in less proportion into the channels, they frequently form small dunes, sand shadows and taluses of sand produced by aeolian deposition along the margins of the channels (Fig. 2B). Moreover, trains of aeolian ripples, resulting from the aeolian reworking of previous fluvial deposits, are frequently found on the floor of some sandy channels.

The interchannel area is dominated by aeolian sedimentation including dunes, protodunes, zibars, and either sandy or muddy interdunes (Fig. 2C),

together with gravelly sandstones and muddy carpets formed by fluvial spills during floods. (Limarino and Martinez, 1992; Tripaldi and Limarino, 2008).

3. Data acquisition and processing

The GPR data were acquired with a pulseEkko Pro system. We employed three pairs of antennae, with nominal frequencies 500 MHz, 250 MHz, and 100 MHz, in constant offset modality. These frequencies provide different resolution of the layers and penetration of the electromagnetic waves in the soil. In general, higher frequencies produce a better resolution of the layers, whereas lower frequencies increase the depth of penetration. The 500 MHz and 250 MHz antennae were mounted on skid plates, whereas the 100 MHz antennae were supported by a cart. The offset was 0.25 m, 0.4 m, and 1 m, respectively. The antennae were hand towed at an average speed of 0.4 – 1.5 km/h, which mostly depended on the slope of the ground. An odometer wheel triggered the acquisition of traces at a regular spacing of 0.04 m, 0.05 m and 0.2 m, respectively. The time window was set to 100 ns, 200 ns, and 300 ns, and the time increment to 0.2 ns, 0.4 ns and 0.8 ns, the system default values. The number of stacking was 16. Larger numbers of this parameter, 32 and 64, were evaluated and discarded since they did not appreciably improve the reflection amplitudes and continuity, and considerably slow down the data acquisition. A measuring tape was used to define the trajectory and length of the survey lines. The positions of the survey lines were measured with a GPS unit Ashtech Promark 2.

The data were processed by applying a sequence of standard GPR procedures (Bonomo et al., 2011; 2012) programmed in Matlab code. In a first

place, a high-pass time filter was applied inside a sliding window to remove low-frequency induction effects of the antennae. Then, fluctuations in the default time-zero reference of the traces, respect to the mean value, were compensated. A high-pass spatial filter was used to remove the direct waves between the antennae, and a mean-amplitude gain curve was applied to compensate wave attenuation. Finally, the data were corrected for topography.

4. Attribute calculation

4.1. Contrast

Contrast is a statistical measure of the amplitude differences in an image or dataset, which has been used both in Seismic and GPR. There are different ways of calculating this attribute; one of the most popular is based on computing a gray-level co-occurrence matrix (GLCM) (Haralick et al., 1973; McClymont, 2008). In this methodology, a moving window is defined, and the intensity difference between neighboring data of the window is calculated along one of its dimensions. The resulting values of intensity difference are divided into categories, and the number of occurrences is calculated for them. The elements of the GLCM matrix, P_{ij} , are defined as the number of data changing from the i th- to the j th-intensity category, normalized by the total number of compared data. As the analysis window is moved through the dataset, a GLCM is obtained for each $\bar{x} - t$.

An estimation of the contrast, I_c , of the data can be obtained from the elements of the GLCM through the following formula (e.g., Zhao et al. 2018):

$$I_c(\bar{x}, t) = \sum_{i,j} P_{ij} (i - j)^2$$

As a consequence, of this definition, the contrast is a dimensionless positive quantity, which takes larger values for more contrasting data and values closer to zero for less contrasting ones.

4.2. Slope and dip

Slope and dip are measures of the orientation of a reflector in a dataset. A way of calculating this orientation at a given position $\vec{x} - t$ of an image is to determine the most coherent plane at this point (e.g., Forte et al., 2012). Different indicators of the waveform similarity can be used to estimate the coherence along the plane, semblance being one of the more frequent between them (Marfurt et al., 1998). Semblance is usually calculated as a function of the orientation of the analysis plane; the orientation that maximizes this variable is considered to produce the plane that best fits the reflection at that point of the image (McClymont et al., 2008; Forte et al., 2012). The slopes of the reflector along and across the survey line, s_x and s_y , which define the direction of the plane, are determined in this way. The dip, θ , respect to a horizontal plane, is then obtained as follows:

$$\theta(\vec{x}, t) = \tan^{-1} \left(\sqrt{s_x^2 + s_y^2} \right)$$

For data represented in time, s_x and s_y have units of ns/m, so $\theta(\vec{x}, z)$ is not strictly an angle. Then, $\theta(\vec{x}, z)$ is a qualitative representation of the dip, and depends on the local value of the propagation velocity. As defined in the previous equation (and as usual in the geological and geophysical nomenclatures), the dip attribute is a positive quantity, whereas the apparent

slopes are positive for reflections dipping along the surface coordinate, and negative otherwise.

4.3. Curvature

Different measures of the curvature of the layers have been defined in the literature to assist the interpretation of the soil structures (Roberts, 2001). The so-called most positive curvature is one of the most usual between them. As occurs with the slope and dip attributes, curvature has been quite frequently applied in Seismic exploration (Chopra and Marfurt, 2007; Abdel-Fattah and Alrefaee, 2014; Ha and Marfurt, 2017; Alrefaee et al., 2018; Kulikowski et al. 2018), but not in GPR (Andrade dos Reis Jr. et al., 2014; Brandes et al., 2018).

A simple way to calculate the curvature is by computing the partial derivatives of the reflection slopes (Roberts, 2001). In particular, the most positive curvature attribute, κ , can be expressed as a function of s_x and s_y , as follows:

$$\kappa(\vec{x}, t) = C_{xx} + C_{yy} + \sqrt{(C_{xx} - C_{yy})^2 + C_{xy}^2}$$

$$C_{xx}(\vec{x}, t) = \frac{1}{2} \frac{\partial s_x}{\partial x}$$

$$C_{xy}(\vec{x}, t) = \frac{\partial s_x}{\partial y} = \frac{\partial s_y}{\partial x}$$

$$C_{yy}(\vec{x}, t) = \frac{1}{2} \frac{\partial s_y}{\partial y}$$

In the case of 2D data, these equations simplify, and the following formula is obtained:

$$\kappa(x,t)=\frac{\partial s_x}{\partial x}$$

The implicit convention in the previous equations is that anticlines and synclines have positive and negative curvature, respectively. Faults and flexures are characterized by curvatures that change the sign from positive to negative, or vice versa, whereas deflation hollows present a positive-negative-positive variation.

Curvature attributes are usually interpreted qualitatively, so their units are not important. The calculation of the curvature involves second derivatives of the data, so it is significantly affected by noise and acquisition artifacts. Smoothing the data before calculating the attribute and averaging multiple estimations of the partial derivatives are common procedures to reduce the fluctuations of the results.

4.4. Parallelism

Parallelism between layers is an attribute less commonly applied to seismic data than the previous ones (Barnes, 2007). To our knowledge, it has not been used with GPR data up to now. To measure the parallelism of a sequence of layers, their orientations have to be compared. Parallelism, P , can be defined from the projections of the vectors normal to the reflections, $\hat{n}(\vec{x}, t)$, on the mean normal direction, $\langle \hat{n} \rangle$ (Barnes, 2007):

$$P(\vec{x}, t) = 100 \langle \hat{n} \cdot \langle \hat{n} \rangle \rangle^2$$

$$\hat{n} = (s_x, s_y, -1) / \sqrt{s_x^2 + s_y^2 + 1}$$

In these equations, \hat{n} is a unitary vector and $\langle \cdot \rangle$ indicates averaging inside a data window. With this definition, parallelism takes values between 0 and 100. The largest values of the attribute correspond to parallel reflections whereas the lowest values correspond to nonparallel or irregular reflections.

4.5. RMS frequency

The root mean square frequency, f_{RMS} , is an indicator of the changes in the frequency spectrum of the GPR pulses due to the attenuation of the waves by different physical processes (Chopra and Marfurt, 2007). It can be calculated by using a sliding time window, as follows:

$$f_{RMS} = \left(\frac{1}{E} \int_0^{\infty} (f A(f))^2 df \right)^{1/2}$$

where f is the frequency, $A(f)$ is the amplitude of the Fourier transform of the data in the window, and E is the total spectral energy

$$E = \int_0^{\infty} (A(f))^2 df$$

Changes in the f_{RMS} indicate that the frequency spectrum of the pulses has been modified in a given media or interface due to, for example, absorption of part of the spectral components.

5. GPR sections

We acquired seven sets of GPR profiles in the fluvial-aeolian interaction field, along dunes, interdunes, muddy plains, and active and inactive fluvial channels (Fig. 1B). With the 500 MHz antennae, a maximum penetration depth

between 0.7 m and 4.3 m was obtained, for the most absorbent (muddy plain bed) and transmissive (sandy environment) media, respectively. This depth was calculated by using a mean velocity of propagation of 0.15 ± 0.05 m/ns, which was calculated by the method of fitting hyperbolae to the diffractions observed in the data sections. With the 250 MHz and 100MHz antennae, we obtained a maximum penetration depth of [1.7 - 5.2] m and [3.5 - 7.7] m, respectively. Although these antennae increased the penetration with respect to the 500 MHz antennae, they significantly reduced the details in the data sections due to the loss of resolution.

Fig. 3A shows a GPR section acquired along a small and isolated dune located in Sector 6 (Fig. 1B), using an antenna frequency of 500 MHz. Several reflections are visible in the radargram (Fig. 3A), which can be characterized according to their different geometries and amplitudes. One of the most important geometric characteristics of the reflections is their apparent dip. Fig. 3B shows the distribution of this attribute when applied to the dataset of Fig. 3A. Three groups of reflectors, with different dips, can be distinguished. Firstly, high-angle reflectors with dip values higher than 20° (red color), a second set with angles between 5° and 20° (yellow color), and a third group of reflectors dipping less than 5° (no color).

Fig. 3C shows the curvature of the reflections inside the first of these groups, which is composed of foreset surfaces. The surfaces are characterized by positive values of the attribute at the top of the foreset (red color), negative values in the middle and lower parts (blue color), and approximately null curvature at the bottom (no color). These characteristics of the pattern of

reflectors, which could be described as tolap and downlap, evidence that grain-fall and grain-flow processes were not the only mechanisms of dune migration. The migration of aeolian ripples was also an active process, at least at the toe of the dunes, as showed by the asymptotic terminations of the reflectors (Pye and Tsoar, 2009).

Reflectors characterized by positive-negative-positive curvature patterns have been also observed in the other profiles of the sector, although much less common than the previous type. Fig. 3D shows an example in which the negative (concave-up) central part of the reflector extends laterally 2.9 m, and the total length of the pattern is 4.7 m, approximately (white circle). Two possible interpretations are compatible with this geometry: the presence of trough cross-bedded sets, indicating periods of high-sinuosity dune migration, and the occurrence of sporadic deflationary events during the construction of the dunes.

Fig. 3E shows the mean frequency of the data inside the third area marked in Fig. 3B. This attribute distinguishes two parts of the structure: the lower part presents lower frequency and higher attenuation (Fig. 3F) than the upper part, which is a characteristic that usually indicates a higher clay content in the soil. Small trenches, and observations along the walls of nearby channels, confirmed this interface, as well as a set of horizontal muddy layers below it, up to 1 m thick, with appreciable contents of clay.

Fig. 3G shows a diagram of the main reflectors and units identified from the analysis of the previous radargrams and attributes. Four sets of reflectors can be observed: the lowest one, a, is located below the altitude 1.5 m and is

characterized by laterally-continue reflectors with approximately null dip (angles below 2° , Fig. 3B), low mean frequency (Fig. 3E) and high attenuation (Fig. 3F). An intermediate area, *b*, which rests on *a* and extends through the altitude interval 1.5 m – 3.0 m, approximately, presents reflection angles between 3° and 12° (yellow color in Fig. 3B), higher frequency and lower attenuation than the previous. The third area, *c*, shows the highest dip angles, which are around 18° , and a geometry that suggests the presence of a cross-bedded set of reflectors, with a characteristic thickness of 1.4 m, approximately. The fourth area, *d*, forms a story above the previous units and is composed of horizontal to low-angle inclined reflections. This story is separated from the intermediate stories (*b-c*) by a slightly irregular (erosive) surface, *e*.

The second type of deposit that is analyzed in this section is commonly observed near of the fluvial channels and consists of aeolian dunes that are located close to each other, but which have different heights and wavelengths, as those illustrated in Fig. 4A. The right dune of the figure exhibits the same two-story pattern previously described for isolated dunes (Fig. 3G), this is, high-angle reflectors in the lower part of the dune (area *a* in Fig. 4B, angles from 3° to 20°) and low-angle reflectors in the upper part (area *b*, angles below 3°). As in the case of the isolated dune illustrated in Fig. 3, both parts of the dunes are separated by a slightly erosive surface, *c* (Figs. 4B and 4C, white arrows). This surface is characterized by low positive (convex-up) values of curvature, except for a portion of surface located near the space between the dunes, which shows negative (concave-up) values of this attribute (Figs. 4C, white arrows). Surface *c* cuts across all the reflectors that form the set *a* and is covered by reflectors *b*, through an onlap arrangement. This geometry suggests a discontinuity in the

sedimentation (represented by surface *c*) and the partial erosion of the dune deposits in the interval *a*, which truncated the foresets in it. A later reactivation in sedimentation produced the onlap disposition of reflectors observed in *b*.

The smaller left dune in Fig. 4, centered at 11 m, approximately, shows inclined reflectors only (angles from 3° to 11°), which are topographically below the height of the deflationary surface that separates the two stories of the right dune (Fig. 4D). This type of association between two dunes with different heights, wavelengths and internal architecture (Fig. 4D), is a common feature in the Guandacol fluvial-aeolian interaction field and, in our opinion, reflects different growth rates of previously deflated dunes.

A more complex type of dunes is illustrated in Fig. 5A. In this example, the presence of the previously described two-story patterns is not so clear, since only the uppermost part of the dune shows an erosive surface overlaid by a thin set of horizontal or low-angle inclined reflectors (*a* in Fig. 5B). Interestingly, the apparent dip attribute exhibits a very intricate pattern of reflectors throughout the rest of the dune, with coexisting high-angle (red color) and low-angle (yellow color) reflectors. In some cases, highly and moderately inclined reflectors dip in opposite directions.

This complexity is better-understood whether the presence of probable deflationary hollows is taken into account. The area marked with *b* in Fig. 5C is characterized by reflections with values of the contrast attribute lower than the surrounding areas, which probably indicates a more homogeneous accumulation of sediments in it (cutoff value 0.5). Moreover, the pattern of surrounding reflections is irregularly interrupted at the borders of this area (Fig.

5C), which seems to indicate deposition into a deflation hollow (dashed line in Fig. 5C). The presence of a few reflections inside the area, which are inclined in opposite directions and towards the interior of the hollow, as well as the high deep/width relation of the hollow could support the hypothesis of a deflation depression (Fig. 5D).

The relation between the aeolian and fluvial terms of the interaction deposits is analyzed from the profile of Fig. 6A, obtained across an active channel. The contrast attribute (Fig. 6B) defines three areas that laterally spread from dunes located in the periphery of the channel to the channel axes. The left interval, *a* in Fig. 6B, corresponds to dune accumulations that show reflectors with lower (yellow color) and more homogeneous contrast distribution than the rest of the section, and that form similar reflection patterns to those found in the aeolian deposits previously analyzed.

The right area comprises fluvial channels, *b* in Fig. 6B, which exhibits the highest reflection contrasts of the section (blue color). Inside the channels, characterized by a lenticular form and an erosive base (*d* in Fig. 6 C and E), the parallelism attribute, shown in Fig. 6D, clearly differentiates a somewhat disordered lower part (no color) and an upper part composed of subparallel reflections (red color). These two patterns could reflect different architectures into the channel belt; the lower part likely corresponds to more incised and lenticular channels than those of the upper part. Indeed, the current bars and channels of the site exhibit shallow relief (less than 1 m of difference between top of the bars and the channel floor) and a limited incision grade.

The third interval of Fig. 6B, c, shows a more heterogeneous distribution of high and low contrast areas than the previous ones and corresponds to a transitional zone in which small dunes appear into the channels (c in Fig. 7A). Concave-up reflectors (as d in Fig. 6C), which correspond to bases of channels, are succeeded by horizontal or low-angle inclined reflectors whose fluvial or aeolian origin is uncertain. In the shallowest parts of the profile, prevail reflectors with scarce relief, which correspond to aeolian protodunes, zibars, and very small dunes (e in Fig. 6C and Fig. 7B). Towards the margin of the channels appears small aeolian talus deposits (f in Fig. 6C and Fig. 7C).

6. Terminology in GPR analysis of the Guandacol fluvial-aeolian field

The nomenclature of GPR stratigraphic analysis has been analyzed in different studies in which the terminology of different types of reflectors, radar bounding surfaces and radar sequences was discussed (Gawthorpe et al., 1983; Neal, 2004; Hugenoltz et al., 2007). In the specific case of GPR analysis of fluvial-aeolian fields, Zabala et al. (2018) identified different types of inclined reflectors grouped into four hierarchy orders of bounding surfaces. This analysis focused on aeolian dunes and followed the guidelines proposed by Brookfield (1977) although with differences in the terminology, that is, the higher is the number of the surface the shorter is its lateral extension. In the specific case of GPR analysis of fluvial-aeolian fields, Zabala et al. (2018) identified different types of reflectors grouped into four hierarchy orders of bounding surfaces.

The analysis of GPR in fluvial-aeolian interaction deposits must be done keeping in mind the complexity of this type of environment, since that the GPR

records not only the dynamic of aeolian and fluvial processes but also the interplay between aeolian and fluvial sedimentation. For example, the recognition of erosion radar bounding surfaces, which were not defined in the above-discussed models, become crucial for the identification of periods of dune degradation owing to fluvial erosion (expansion of the fluvial term), versus dune and interdune growing (expansion of the aeolian term). For this reason, we slightly modified the above discussed stratigraphic models, recognizing radar surfaces, radar bounding surfaces, and radar packages (Figs. 8, 9).

7.1. Radar surfaces

In this paper, radar surfaces are defined in a more restricted way than previously used by Neal (2004) and Hugenholtz et al. (2007) for describing the reflectors that show parallel or subparallel configurations. Therefore, the surfaces that bound sets of radar surfaces are not included in this category, and are referred to as radar bounding surfaces.

In the fluvial-aeolian deposits of the Guandacol area, four main types of radar surfaces were recognized (Fig. 8): 1) Horizontal, 2) Inclined with basal tangential contact, 3) Inclined with basal angular contact and, 4) Trough-shaped reflectors. It is worth noting that GPR images only detect those surfaces that show contrast in permittivity above the sensitivity threshold of the instrument, and therefore, only part of the radar surfaces are detected.

Horizontal radar surfaces are the dominant reflector in sandy interdune areas and consist of laterally continuous parallel or subparallel reflectors that correspond to laminations developed into the sandy deposits. The lamination probably results from migration of aeolian ripples trains, which represent the

dominant bedform in the interdunes. The existence of subparallel, and in some cases low-angle reflectors, likely reflect the slightly undulating microtopography of the interdunes and the climbing of ripples over the surface of the sand shadows and zibars.

Another type of horizontal radar surface occurs in the muddy interdune areas, which shows tabular form and considerable lateral continuity, but in this case, horizontal reflectors are diffuse or at least not so clearly marked as in the sand deposits (Fig. 3A,B) . Frequently, the muddy horizon appears partially obscured, either by the very high absorption of electromagnetic waves in the mud, or owing to the lamination was poorly developed or highly bioturbated. Horizontal radar surfaces also appear associated with the filling of some fluvial channels indicating that aggradation was dominated by very low-relief bars and channel lag accumulations (Fig. 6D,E).

Inclined tangential and angular basal contact radar surfaces dominate in the lower part of the dune deposits and represent foresets formed during the dune migration. The difference between tangential and angular basal contact of the surface reflects changes in the mechanism of dune migration, while tangential foresets suggest that the climbing of aeolian ripples was an active process during the migration of the dunes, angular basal contacts likely indicate that grain-flow and grainfall processes prevailed over the ripple migration.

Trough-shaped reflectors are found in both aeolian and fluvial accumulations. In the first case, this type of reflector could indicate the presence of barchan dunes or barchanoid ridges while that in fluvial channels would indicating cut and fill structures or high-sinuosity bars.

7.2. Radar bounding surfaces

Following the terminology used by Neal et al. (2001), the bounding radar surfaces separate sets of radar surfaces. In this way, radar bounding surfaces have a similar significance to the bounding surfaces described in aeolian deposits by Brookfield (1977) and Kocurek (1981, 1991), and in fluvial environments by Miall (1985, 1988). Four types of radar bounding surfaces are recognized (Fig. 8): 1) plane horizontal, 2) plane inclined, 3) concave-up (erosive) and 4) convex-up.

Both horizontal and inclined radar bounding surfaces occur in the aeolian term of the interaction deposits. Plane horizontal bounding surfaces dominate in the interdune area while a plane inclined surfaces are more common in dunes.

Concave-up radar bounding surfaces are commonly identified at the base of fluvial channels and represent erosive surfaces of different lateral continuity and morphology. Surfaces exhibiting short lateral persistence (from 2m to 10 m) are linked to the floor of individual channels into the channel belt, whereas those surfaces with high lateral continuity (several tens of meters) probably mark the base of the channel belts. On the other hand, small concave-up radar bounding surfaces, identified in some dune accumulations, may correspond to the bottom of small blowouts carved into the dunes.

Finally, convex-up surfaces are found in both aeolian and fluvial deposits; in the first case, the surface probably reflects the morphology of partially deflated dunes or the depositional surface of preserved aeolian mesoforms (zibars and protodunes, Langford and Chan, 1988; Tripaldi and Limarino, 2005, 2008). In fluvial deposits, convex-up radar bounding surfaces correspond to the top of

small bars preserved into the channels and correspond to the third-order bounding surfaces of Miall (1985).

7.3. Radar packages

We use the term radar packages, in a similar way Neal (2004) and Hugenholz et al. (2007), for including genetically related strata, limited at top and bottom by radar bounding surfaces. We recognized seven radar packages (Fig. 9), which correspond to different types of dunes and architectural elements in fluvial channels.

Radar package 1 consists of both inclined tangential and angular radar reflectors limited by plane inclined surfaces that cut along the foreset. The bounding surfaces and foreset dip in opposite directions, which suggest that this radar package resulted from the climbing of dunes trains along the windward face of dunes. If the radar surfaces and bounding reflector were inclined in the same direction, the dunes could have descended along the leeward front of previously formed and fixed dunes. However, this situation, although frequent in aeolian-fluvial interaction areas, was not identified in the Guandacol field.

The alternation of tangential and angular radar surfaces indicate that the mechanisms of dune migration changed from grainfall-grainflow to grainfall-aeolian ripple migration when the slope of the leeward-face of dunes diminished (Hunter, 1977, 1985; Kocurek and Dott, 1981).

Radar package 2 differs in the presence of trough-shaped radar surfaces that are constrained by plane inclined surfaces and probably reflects the climbing of sinuous dunes (including barchans). In some cases, radar packages

2 are covered by radar packages 1, indicating the superposition of dunes of low-sinuosity over those of high-sinuosity.

Radar package 3 is composed of thin bundles of inclined parallel radar surfaces that, in most cases, exhibit angular basal terminations. Each bundle is limited by low-angle plane inclined or slightly convex-up radar bounding surfaces. A distinct feature of this radar package is the scarce lateral continuity of the bounding surfaces which usually intersect each other, originating a characteristic wedge-like shape. Taking into account the thin thickness of the sets, the limited lateral continuity of the radar surfaces and the presence of convex-up bounding surfaces, the package 3 indicates the migration of aeolian mesoforms (protodunes) or the stacking of fixed aeolian mesoforms (zibars) over the dune surface (Nielson and Kocurek, 1986; Tripaldi and Limarino, 2008).

Radar package 4 consists of either horizontal or low-angle radar surfaces limited at the bottom by planar horizontal or slightly inclined radar bounding surfaces, which usually serve as a sharp separation with the underlying radar packages 1 and 2. The top of this radar package corresponds to the present-day dune morphology forming a convex-up top surface (Fig. 9).

The reflectors that form the radar package 4 most probably originated after the partial deflation of a dune body, creating a plane horizontal or slightly inclined, represented in the basal radar bounding surface. Then stacking of laminae formed by migration of aeolian ripples would have formed the flat and low-angle lamination, responsible for the horizontal (or slightly inclined) radar surfaces that form this package.

Radar package 5 corresponds to a tabular horizon, of about 40 cm thick, entirely composed of muddy, poorly-laminated sediments that show the diffuse horizontal disposition of radar surfaces. The upper limit is a plane and flat radar bounding surface while the lower limit is somewhat diffuse owing to a complex series of interfering diffractions developed at the base of the muddy bed. The radar profiles demonstrate that radar package 5 is continuous in the whole of the area and serve as the substratum of the major part of the dunes in the survey area. The muddy composition of the interval and its lateral continuity suggest a period of flooding of the aeolian field, probably related to more humid conditions.

Radar package 6 is characteristic of the infill of fluvial channels and consists on slightly inclined and irregular radar surfaces that, in some cases, pass upward to parallel horizontal reflectors. The base of the package corresponds to high-relief concave-up radar bounding planes while a smooth flat or low-relief irregular surface form the top. A highlighted feature is the occasional presence of bundles of convex-up minor surfaces show scarce lateral continuity.

The radar package 6 exhibits the different architectures showed by the fluvial channels. Firstly, the concave-up radar bounding surface, with high erosive base, represents the base of individual channels while the convex-up surfaces are interpreted as the preserved form of the bars.

Finally, radar package 7 forms the upper part of the fluvial system in the Guandacol area and is composed of the superposition of parallel to subparallel horizontal radar reflectors. In this package concave-up bounding radar, surfaces are missing, and only some convex-up bounding surfaces interrupt the

monotonous horizontal disposition of the reflectors. The radar package 7 is interpreted as the infill of low-relief channels in a highly aggradational stage of the fluvial system. The sporadic presence of convex-up bounding surfaces indicates the preservation of the morphology of some bars.

8. Discussion

Radar packages allow identifying not only the characteristics of the different geoforms present in the Guandacol fluvial-aeolian interaction field but also the evolution in space and time of this depositional system and its stratigraphy. Fig. 10 shows a schematic representation of the fluvial-aeolian interaction system, the relation with radar packages, and the internal structure of the dunes.

The continuous muddy horizon (radar package 5) separates two groups of dune accumulation (G1 and G2, in Fig. 10A, Fig. 11), and probably points out a period of humidity increase that promoted firstly to the formation of muddy wet interdunes and later the flooding of interdunes, in a similar way to the described by Langford and Chan (1988). The presence of abundant roots, and poorly developed paleosols in the muddy horizon, clearly suggest the presence of wet overbank interdunes, probably connected to the incision of the fluvial channels (Langford and Chan, 1988).

The characteristics of the aeolian deposits located below the muddy level are masked by interfering reflection produced by the fine-grained bed. But in the cut of some fluvial terraces, the incised channels show fine-grained sandstones below the muddy bed (Fig. 10). The good sorting of these sandstones, together with the presence of delicate cross-bedded sets, suggest that had two periods of aeolian sedimentation, the lower (G1 in Fig. 10A) predated the climate

amelioration represented in the muddy bed, and the upper (G2 in Fig. 10A) points out the reinstallation of semiarid climate.

The dune deposits that overlay the muddy horizon pass laterally to the interdune accumulations characterized by horizontal parallel, or low-angle inclined radar surfaces (radar package 4, Fig. 12C). This package reflects the migration of successive trains of aeolian-ripples which owing to the low-angle of ripple-climbing form horizontal or slightly inclined lamination. In our opinion, the number and quality of reflectors in the dry interdunes principally depend on the type of aeolian ripple that migrated. In the case of very fine- and fine-grained sand in the interdune setting, the major part of the sand is transported by impact-projection, which results in a very fine and homogeneous lamina.

On the contrary, if the sand includes a significant population of medium and coarse-grained sand, some of the coarse-particles are transported by creeping forming a slightly thicker and less texturally homogeneous lamina (up to 1 cm).

The alternation of lamina sets dominated by impact-projection and clast-creeping, versus those where the impact projection is the unique transport mechanism, produce changes in the thickness, packing, and texture of the lamination, favoring the clearer expression of the reflector (radar package 4).

The internal structure of the dunes can be divided into two terms (Fig. 10C). The first that become visible at the lower part of the dunes reflect active migration of dunes, forming both inclined tangential and angular radar reflectors (radar packages 1, Fig. 12A) or trough-shaped radar surfaces (radar packages 2 and 3, Fig. 12B). On the contrary, the upper part of the dunes is made up by the stacked sets of horizontal or slightly inclined parallel radar surfaces (radar

package 4, Figs. 10C, 12A). The change of the radar packages 1 and 2 respect to package 4 is generally marked by a plane horizontal or slightly inclined surface (in some cases as a convex-up reflector, Fig. 10C). This surface is here interpreted as a deflationary level that indicates a period of partial destruction of the dunes. It is possible that this surface could be correlated in time with the previously considered flooding of the interdune areas (muddy interval, package 5, Fig. 13).

The fluvial term of the analyzed succession is represented in the radar packages 6 and 7, evidencing two different architectures in the fluvial system (Figs. 10, 13). The radar package 6 dominates in the lower part of the fluvial record (below 3 m in Fig. 6) and is characterized by the presence of high-relief concave-up radar bounding planes that mark the base of incised channels that pass upward to convex-up surfaces that correspond to the preserved top of bars.

In the case of the radar package 7, that dominate at shallow depth channels, is composed of the stacking of parallel and subparallel horizontal radar reflectors, without incised channels marked by concave-up radar bounding surfaces (Fig. 6). The change in the radar packages from package 6 to package 7 indicates an increase in the aggradation of the fluvial system and decreasing in the relief of bars.

A model that related the radar packages with the evolution of the fluvial-aeolian interaction system is shown in Fig. 13. In this scheme, and according to observations along fluvial terraces, took place an active dune migration stage previously to the formation of the muddy bed, but it was not possible to obtain

accurate GPR images for this interval. The muddy bed (radar package 5) is interpreted as the consequence of the flooding of interdunes (high water-table conditions) in response to climate amelioration (Figs. 11, 13). It is interesting to speculate that under this humid climate, the fluvial systems could have had high energy and form the incised channels and high-relief bars represented in the radar package 6 (Fig. 13).

Seemingly, the climate amelioration was followed again by arid and semiarid conditions, which promoted a new stage of dune growth and migration (Fig. 13). At this time, the radar configurations (radar packages 1, 2 or 3) depended on the dune type and the relation between aeolian megaforms (dunes) and mesoforms (protodunes and small dunes).

An episode of dune deflation was recorded in the deflationary surface that separates radar packages 1, 2, and 3 from radar package 4. Above this surface, dunes began to grow again, but from this time aeolian ripple migration becomes the dominant mechanism for the dune construction, probably as a consequence of limited supply of sand (Fig. 13).

9. Conclusions

1. Attribute calculation from the 2D data sections improves the interpretation of the subsurface by quantifying and making evident properties of the reflection patterns that characterize the units. In particular, the apparent dip of the reflectors proves to be useful for identifying and characterizing packages of reflectors with different inclinations. The curvature attribute shows helpful for identifying and classifying concave and convex reflectors, as deflation surfaces and bars, as well as giving details of the reflector terminations against other

reflectors and variations along them. Parallelism allows distinguishing between units with parallel layers and more disordered geometries and, as the previous attributes, shows the advantage of being independent of the reflectivity of the components. The RMS frequency is useful for distinguishing units with different type of absorption of the spectrum of electromagnetic waves. Finally, the contrast attribute helps to distinguish units with distinct reflectivity, as the aeolian and fluvial terms of the investigated channel areas.

2. The GPR methodology applied in this paper is useful for studying both terms that form the fluvial-aeolian interaction deposits. It allows describing not only the internal structure of the aeolian accumulations (different types of dunes, dry interdunes, and wet interdunes) but also showing differences in the architecture of fluvial channels.

3. The radar packages offer a conceptual model for analyzing the significance of the vertical and lateral changes observed in the interaction fluvial-aeolian environment and permit to reconstruct the stratigraphy and recent evolution of this environment.

4. In the case of the Guandacol area, the fluvial-aeolian interaction system shows high variability in space and time, reflected by changes in the type of radar packages. Probably during humid periods, interdunes were wider (radar package 5); conversely, the semiarid conditions produced the reactivation of the dunes (radar packages 1, 2 and 3) and the prevalence of the aeolian term above the fluvial terms.

5. The continuous presence of horizontal or slightly inclined reflectors in the upper part of the dunes (radar package 4), indicates that the principal

mechanism for their growth was the climbing of aeolian ripples, associated to grain-fall along the leeward face of the dunes. These mechanisms are dominant at present and likely indicate an intermediate situation between humid and arid conditions.

6. The wet interdunes (radar package 5) point out a period of climate amelioration and probably correlate with the deflationary surface that separates the radar packages 1, 2 and 3 (active dune migration) from package 4 (dune stabilization or low migration rate). Both interdunes and deflationary surfaces mark a significant discontinuity that can be used as a key surface for correlation with an indubitable genetic significance.

7. Two architectures of fluvial deposits were identified using radar packages. Radar package 6 indicates the presence of high-incised channels while radar package 7 suggests shallow streams with low relief of the alluvial plains.

Acknowledgments. We are grateful to Klaus Schroeder and Dr. Sergio Marensi for their assistance in the field and their helpful discussions. We are also grateful to the reviewers for their useful suggestions. This research was supported by the Agencia Nacional de Promoción Científica y Tecnológica PICT 2014/1613.

References

- Abdel-Fattah, M., Alrefaee, H., 2014. Diacritical Seismic Signatures for Complex Geological Structures: Case Studies from Shushan Basin (Egypt) and Arkoma Basin (USA). *International Journal of Geophysics* 2014, 1-11. <https://doi.org/10.1155/2014/876180>.
- Al-Masrahy, M.A., Mountney, N.P., 2015. A classification scheme for fluvial-aeolian system interaction in desert-margin settings. *Aeolian Research* 17, 67-88.
- Alrefaee, H., Ghosh, S., Abdel-Fattah, M., 2018. 3D seismic characterization of the polygonal fault systems and its impact on fluid flow migration: An example from the Northern Carnarvon Basin, Australia. *Journal of Petroleum Science and Engineering*, 167 120–130.
- Andrade dos Reis Jr., Lopes de Castro, J., Silva de Jesús, T., Lima Filho, F., 2014. Characterization of collapsed paleocave systems using GPR attributes. *Journal of Applied Geophysics* 103, 43–56.
- Barnes, A., 2007. Redundant and useless seismic attributes. *Geophysics* 72, 33–38.
- Basilici, G., Dal'Bó, P.F.F., 2014. Influence of subaqueous processes on the construction and accumulation of an aeolian sand sheet. *Earth surface processes and landforms* 39, 1014-1029.
- Bongiolo, D.E., Scherer, C.M., 2010. Facies architecture and heterogeneity of the fluvial–aeolian reservoirs of the Sergi formation (Upper Jurassic), Recôncavo Basin, NE Brazil. *Marine and Petroleum Geology* 27, 1885-1897.

- 752 Bonomo, N., de la Vega, M, Martinelli, P., Osella, A, 2011. Pipe-flange detection
753 with GPR. *Journal of Geophysics and Engineering* 8, 35-45.
- 754 Bonomo, N., Osella, A., Martinelli, H., de la Vega, M., Cocco, G., Letieri, F.
755 and Frittegotto, G., 2012. Location and characterization of the Sancti Spiritus
756 Fort from geophysical investigations. *Journal of Applied Geophysics* 83, 57–
757 64.
- 758 Brandes, C., Igel, J., Loewer, M., Tanner, D., Lang, J., Müller, K., Winsemann,
759 W., 2018. Visualisation and analysis of shear-deformation bands in
760 unconsolidated Pleistocene sand using ground-penetrating radar:
761 Implications for paleoseismological studies. *Sedimentary Geology* 367, 135–
762 145.
- 763 Bristow, C.S., Jones, B.G., Nanson, G.C., Hollands, C., Coleman, M., Price, D.
764 M., 2007. GPR surveys of vegetated linear dune stratigraphy in central
765 Australia: Evidence for linear dune extension with vertical and lateral
766 accretion. *Special Papers-Geological Society of America* 432, 19-33.
- 767 Brookfield, M. E., 1977. The origin of bounding surfaces in ancient aeolian
768 sandstones. *Sedimentology* 24, 303-332.
- 769 Bullard, J. E., Livingstone, I., 2002. Interactions between aeolian and fluvial
770 systems in dryland environments. *Area* 34, 8-16.
- 771 Bullard, J. E., McTainsh, G. H., 2003. Aeolian-fluvial interactions in dryland
772 environments: examples, concepts and Australia case study. *Progress in*
773 *Physical Geography* 27, 471-501.

- 774 Chopra, S., Marfurt, K., 2007. Seismic Attributes for Prospect Identification and
775 Reservoir Characterization. SEG Geophysical Developments Series No. 11.
776 pp. 464.
- 777 Ercoli, M., Pauselli, C., Cinti, F.R., Forte, E., Volpe, R. 2015. Imaging of an
778 active fault: Comparison between 3D GPR data and outcrops at the
779 Castrovillari fault, Calabria, Italy. Interpretation 3, SY57-SY66.
- 780 Forte, E., Pipan, M., Casabianca, D., Di Cuia, R., Riva, A., 2012. Imaging and
781 characterization of a carbonate hydrocarbon reservoir analogue using GPR
782 attributes. Journal of Applied Geophysics 81, 76-87.
- 783 Fu, T., Tan. L., Wu, Y., Wen, Y., Li, D., Duan J., 2018. Quantitative analysis of
784 ground penetrating radar data in the Mu Us Sandland. Aeolian Research 32,
785 218–227.
- 786 Gawthorpe, R.L., Collier, R.E.L., Alexander, J., Leeder, M., Bridge, J.S., 1993.
787 Ground penetrating radar: Application to sandbody geometry and
788 heterogeneity studies. Geological Society Special Publication 73, 421–432.
- 789 Geerdes, I., Young, R., 2007. Spectral decomposition of 3D ground-penetrating
790 radar data from an alluvial environment. The Leading Edge 26, 1024-1030.
- 791 Gil, H., Luzón, A., Soriano, M. A., Casado, I., Pérez, A., Yuste, A., Pueyo, E.,
792 Pocoví, A., 2013. Stratigraphic architecture of alluvial–aeolian systems
793 developed on active karst terrains: An Early Pleistocene example from the
794 Ebro Basin (NE Spain). Sedimentary Geology 296, 122-141.

- 795 Girardi, J. D., and Davis, D. M. 2010. Parabolic dune reactivation and migration
796 at Napeague, NY, USA: Insights from aerial and GPR imagery.
797 *Geomorphology*, 114(4), 530-541.
- 798 Ha, T., Marfurt, K., 2017. Seismic reprocessing and interpretation of a fractured-
799 basement play: Texas Panhandle. *Interpretation* 5, SK179-SK187.
- 800 Haralick, R., Dinstein, I., Shanmugam, K., 1973. Textural Features for Image
801 Classification. *IEEE Transactions on Systems, Man and Cybernetics* 3, 610-
802 621.
- 803 Herries, R.D., 1993. Contrasting styles of fluvial–aeolian interaction at a
804 downwind erg margin: Jurassic Kayenta–Navajo Transition, Northeastern
805 Arizona, USA. *Geological Society Special Publication* 73, 199–218.
- 806 Hollands, C.B., Nanson, G.C., Jones, B.G., Bristow, C.S., Price, D.M., Pietsch,
807 T.J., 2006. Aeolian–fluvial interaction: Evidence for Late Quaternary channel
808 change and wind-rift linear dune formation in the northwestern Simpson
809 Desert, Australia. *Quaternary Science Reviews* 25, 142-162.
- 810 Hugenholtz, C.H., Moorman, B.J., Wolfe, S.A., 2007. Ground penetrating radar
811 (GPR) imaging of the internal structure of an active parabolic sand dune.
812 *Special Papers Geological Society of America* 432, 35-45.
- 813 Hunter, R. E. (1977). Basic types of stratification in small eolian dunes.
814 *Sedimentology*, 24(3), 361-387.
- 815 Hunter, R. E. (1985). A kinematic model for the structure of lee-side deposits.
816 *Sedimentology*, 32(3), 409-422.

- 817 Iriondo, M.H., 1997. Models of deposition of loess and loessoids in the Upper
818 Quaternary of South America. *Journal of South American Earth*
819 *Sciences* 10, 71-79.
- 820 Kocurek, G., 1981. Significance of interdune deposits and bounding surfaces in
821 aeolian dune sands. *Sedimentology* 28, 753-780.
- 822 Kocurek, G., 1991. Interpretation of ancient eolian sand dunes. *Annual Review*
823 *of Earth Planet Sciences* 19, 43–75.
- 824 Kocurek, G., Dott, R. H. 1981. Distinctions and uses of stratification types in the
825 interpretation of eolian sand. *Journal of Sedimentary Research*, 51(2), 579-
826 595.
- 827 Kulikowski, D, Amrouch, K., Burgin, H, 2018. Mapping permeable subsurface
828 fracture networks: A case study on the Cooper Basin, Australia. *Journal of*
829 *Structural Geology* 114, 336–345.
- 830 Kumar, P. , Sain, K., 2018. Attribute amalgamation-aiding interpretation of faults
831 from seismic data: An example from Waitara 3D prospect in Taranaki basin
832 off New Zealand. *Journal of Applied Geophysics* 159, 52-68.
- 833 Langford, R.P., Chan, M.A., 1988. Fluvial-aeolian interactions: Part II, ancient
834 systems. *Sedimentology* 36, 1037-1051.
- 835 Limarino, C.O., Martínez, G., 1992. Caracterización textural de algunas
836 mesoformas eólicas de ambientes semidesérticos en el Bolsón de
837 Guandacol. IV Reunión Argentina de Sedimentología. *Actas* II, 295-302.

- 838 Liu, B., Coulthard, T.J., 2015. Mapping the interactions between rivers and sand
839 dunes: implications for fluvial and aeolian geomorphology. *Geomorphology*
840 231, 246–257.
- 841 Liu, B., Coulthard, T.J., 2017. Modelling the interaction of aeolian and fluvial
842 processes with a combined cellular model of sand dunes and river systems.
843 *Computers and Geosciences* 106, 1-9.
- 844 Marfurt, K., Kirlin, R., Lynn Farmer, S., Bahorich, M., 1998. 3-D seismic
845 attributes using a semblance-based coherency algorithm. *Geophysics* 63,
846 1150–1165.
- 847 McClymont, A.F., Green, A.G., Streich, R., Horstmeyer, H., Tronicke, J., Nobes,
848 D.C., Pettinga, J., Campbell, J., Langridge, R., 2008. Visualization of active
849 faults using geometric attributes of 3D GPR data: An example from the
850 Alpine Fault Zone, New Zealand. *Geophysics* 73, 11-23.
- 851 Meadows, N.S., Beach, A., 1993. Structural and climatic controls on facies
852 distribution in a mixed fluvial and aeolian reservoir: The Triassic Sherwood
853 Sandstone in the Irish Sea. In: C.P. North y D.J. Prosser, (Eds.),
854 *Characterization of Aeolian and Fluvial Reservoirs*. Geological Society
855 London, Special Publications, 73, pp. 247-264.
- 856 Mehl, A., Tripaldi, A., Zárata, M., 2018. Late Quaternary aeolian and fluvial-
857 aeolian deposits from southwestern Pampas of Argentina, southern South
858 America. *Palaeogeography, Palaeoclimatology, Palaeoecology* 511, 280-
859 297.

- 860 Miall, A.D., 1985. Architectural-element analysis: a new method of facies
861 analysis applied to fluvial deposits. *Earth Science Reviews* 22, 261-308.
- 862 Miall, A.D., 1988. Architectural elements and bounding surfaces in fluvial
863 deposits: anatomy of the Kayenta Formation (Lower Jurassic), southwest
864 Colorado. *Sedimentary Geology* 55, 233-262.
- 865 Moysey, S., Knight, R.J., Jol, H.M., 2006. Texture-based classification of
866 ground-penetrating radar images. *Geophysics* 71, K111-K118.
- 867 Neal, A., Roberts, C.L., 2001. Internal structure of a trough blowout, determined
868 from migrated ground-penetrating radar profiles. *Sedimentology* 48, 791-
869 810.
- 870 Neal, A., Richards, J., Pye, K., 2002. Structure and development of shell
871 cheniers in Essex, southeast England, investigated using high-frequency
872 ground-penetrating radar. *Marine Geology* 185, 435-469.
- 873 Neal, A., 2004. Ground-penetrating radar and its use in sedimentology:
874 principles, problems and progress. *Earth Science Reviews* 66, 261-330.
- 875 Nielson, J., Kocurek, G. 1986. Climbing zibars of the Algodones. *Sedimentary*
876 *Geology*, 48(1-2), 1-15.
- 877 Nobes, D., Jol, H., Duffy, B., 2016. Geophysical imaging of disrupted coastal
878 dune stratigraphy and possible mechanisms, Haast, South Westland, New
879 Zealand. *New Zealand Journal of Geology and Geophysics* 59, 426-435,
880 <https://doi.org/10.1080/00288306.2016.1168455>.

- 881 Pedersen, K., and Clemmensen, L. B. 2005. Unveiling past aeolian landscapes:
882 a ground-penetrating radar survey of a Holocene coastal dunefield system,
883 Thy, Denmark. *Sedimentary Geology*, 177(1-2), 57-86.
- 884 Pye, K., Tsoar, H., 2009. Mechanics of aeolian sand transport. In *Aeolian Sand*
885 *and Sand Dunes*, 99-139. Springer, Berlin, Heidelberg.
- 886 Roberts, A., 2001. Curvature attributes and their application to 3D interpreted
887 horizons. *First Break* 19, 85-100.
- 888 Roskin, J., Tsoar, H., Porat, N., Blumberg, D.G., 2011. Palaeoclimate
889 interpretations of Late Pleistocene vegetated linear dune mobilization
890 episodes: evidence from the northwestern Negev dunefield. *Isr. Quaternary*
891 *Science Reviews* 30, 3364–3380.
- 892 Roskin, J., Blumberg, D. G., and Kutra, I. 2014. Last millennium development
893 and dynamics of vegetated linear dunes inferred from ground-penetrating
894 radar and optically stimulated luminescence ages. *Sedimentology*, 61(5),
895 1240-1260.
- 896 Spalletti, L.A., Veiga, G.D., 2007. Variability of continental depositional systems
897 during lowstand sedimentation: an example from the Kimmeridgian of the
898 Neuquen basin, Argentina. *Latin American Journal of Sedimentology and*
899 *Basin Analysis* 14, 85–104.
- 900 Spalletti, L.A., Limarino, C.O., Piñol, F.C., 2010. Internal anatomy of an erg
901 sequence from the aeolian-fluvial system of the De La Cuesta Formation
902 (Paganzo Basin, northwestern Argentina). *Geological Acta* 8, 431-447.

- 903 Tripaldi, A., 2002. Sedimentología y evolución del campo de dunas de Médanos
904 Grandes (provincia de San Juan, Argentina). *Latin American Journal of*
905 *Sedimentology and Basin Analysis* 9, 65-82.
- 906 Tripaldi, A., Limarino, C.O., 2005. Vallecito Formation (Miocene): The evolution
907 of an eolian system in an Andean foreland basin (northwestern Argentina).
908 *Journal of South American Earth Sciences* 19, 343-357.
- 909 Tripaldi, A. y Limarino, C.O., 2008. Ambientes de interacción eólica-fluvial en
910 valles intermontanos: ejemplos actuales y antiguos. *Latin American Journal*
911 *of Sedimentology and Basin Analysis* 15, 43-66.
- 912 Veiga, G.D., Spalletti, L.A., Flint, S., 2002. Aeolian/fluvial interactions and high-
913 resolution sequence stratigraphy of a non-marine lowstand wedge: The Avilé
914 Member of the Agrio Formation (Lower Cretaceous), central Neuquén Basin,
915 Argentina. *Sedimentology* 49, 1001-1019.
- 916 Wang, S., Yuan, S., Wang, T., Gao, J., Li, S., 2018. Three-dimensional
917 geosteering coherence attributes for deep-formation discontinuity detection.
918 *Geophysics* 83, O105-O113.
- 919 Zabala Medina, P., Bonomo, N., Osella, A. M., Salvó Bernárdez, S.C., Limarino,
920 C.O., 2018. GPR prospecting of fluvial-eolian interaction deposits in the
921 Bermejo Valley, NW Argentina. 24th European Meeting of Environmental
922 and Engineering Geophysics. September 2018, Porto, Portugal. 143674.
923 <https://doi.org/10.3997/2214-4609.201802474>.

924 Zhao, W., Forte, E., Fontolan, G., Pipan, M., 2018. Advanced GPR imaging of
925 sedimentary features: integrated attribute analysis applied to sand dunes.
926 Geophysical Journal International 213, 147-156.

927

Journal Pre-proof

FIGURE CAPTIONS

Fig. 1: A. Satellite image of the Guandacol Valley. Numbered circles indicate the positions of the investigated sectors. A rectangular frame indicates the area enlarged in Fig.1B. B. Detail of the investigated sectors. The yellow lines indicate the positions of the GPR profiles.

Fig. 2: A. General view of the fluvial-aeolian interaction system showing both ephemeral channels and interchannel areas dominated by dunes and aeolian mesoforms. B. Example of a talus deposit formed by aeolian action along the margin of the channel. C. Small dune showing the aeolian-ripple migration parallel to the crest and along the lee side of the dune.

Fig. 3: A. GPR data section acquired across a small isolated dune (wester profile in 6, Fig. 1). The antenna frequency is 500 MHz. B. Apparent dip. The rectangles Fig. C, Fig. D and Fig. E indicate areas illustrated in the next figures. C. Curvature of the reflectors in one of these areas. D. Curvature of the reflectors in another of the areas marked in B. The circle indicates a reflector that is characterized by a positive-negative-positive pattern. E. RMS frequency of the data in the third area marked in B. F. Mean reflection amplitude as a function of the travelttime. G. Diagram of the relevant surfaces and units of the profile. The labels a to e indicate sets of reflectors with different geometries and attribute characteristics.

Fig. 4: A. GPR profile across a pair of close dunes with different heights and wavelengths (easter profile in 6, Fig. 1). Fig. B and Fig. C indicate areas illustrated in the next figures. B. Apparent dip for the data in one of these areas. The labels a and b indicate sets of reflectors with different dip

characteristics. Reflector c separates a from b. C. Curvature in one of the areas marked in A. The white arrows point out an erosive surface probably related to deflationary processes. D. Diagram of the surfaces and units identified along the profile.

Fig. 5: A. GPR data section acquired across a type of dunes that shows irregular contours, including important depressions (profile 5 in Fig. 1). The rectangle indicates the area shown in the following figure. B. Apparent dip attribute. The upper story observed in the previous profiles manifests here through the small area a. C. Contrast (cutoff value = 0.5). The reflection pattern is less contrasting in the encircled area than in the surrounding areas, indicating a discontinuity. D. Diagram of the surfaces and packages identified along the profile. A deflation depression has been indicated (b), as well as sets of reflectors with different dip characteristics (a, c-d).

Fig. 6: A. GPR data section acquired through an active fluvial channel (profile 3 in Fig. 1). B. Reflection contrast, labels a - c indicate intervals with different reflection characteristics. C. Parallelism attribute on the zoom view marked in B. D. Interpretation on the zoom view marked in B. E. Diagram of the surfaces and packages identified along the profile.

Fig. 7: A. A general view of the zone in which the GPR profile of Fig. 6 was acquired, showing the lateral transition from aeolian dunes preserved in overbank environment (a), to channels with abundant aeolian mesoforms and channels dominated by fluvial bars, B. Small protodunes and sand shadows into the fluvial channels. C. A vertical section in a terrace that

exhibits recent fluvial conglomerates covered by aeolian dune accumulations.

Fig. 8: Schematic representation of the radar surfaces and radar bounding surfaces identified in this paper.

Fig. 9: Principal radar packages identified in the fluvial-aeolian interaction field of the Guandacol valley. For explanation see the text.

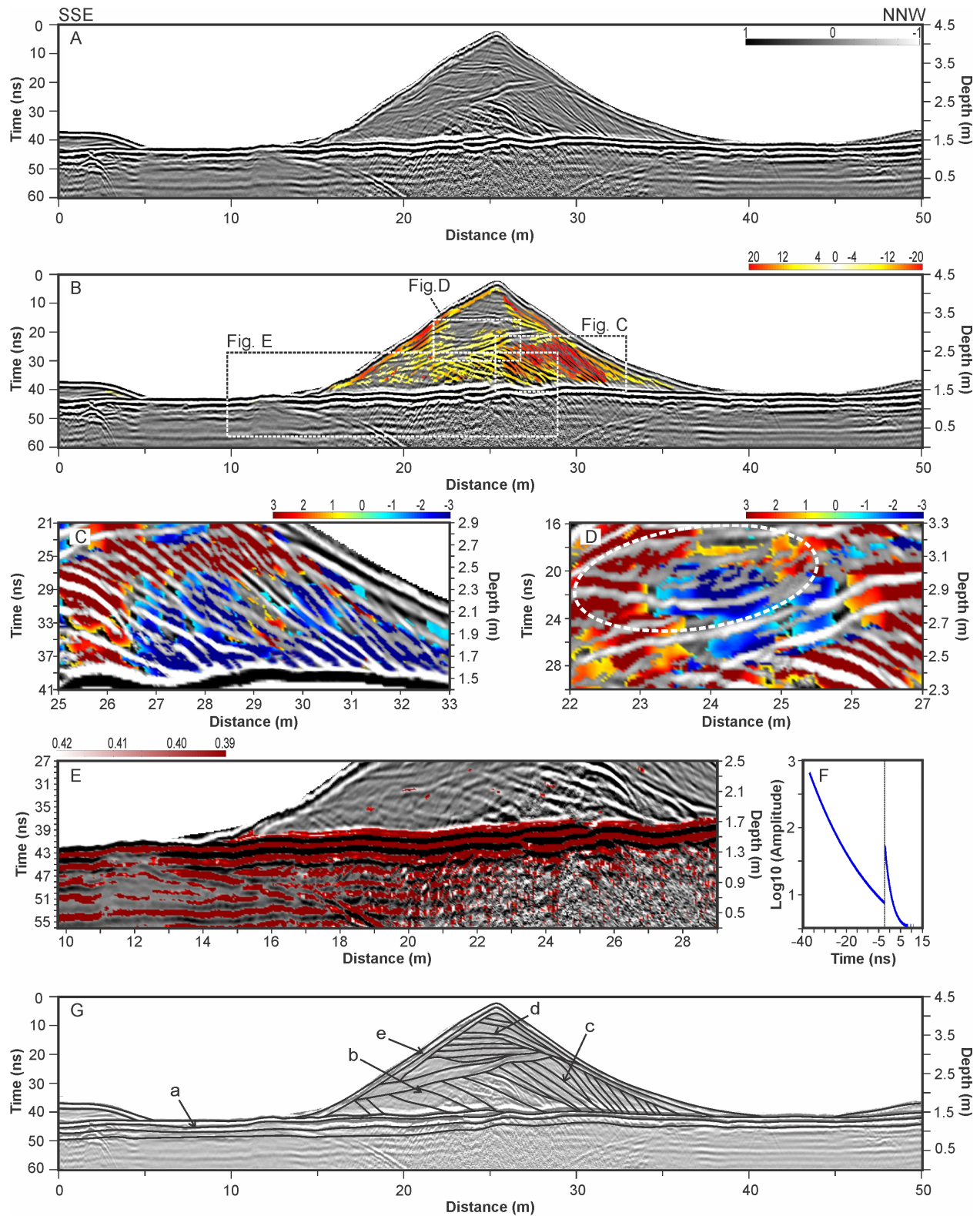
Fig. 10: Relation between principal geoforms (A) and radar packages (B) in the studied area. In C the more common internal structure of the dunes is represented, note that a deflationary surface separates well developed cross-bedded sets (radar packages 1,2 and 3) from horizontal or low angle-inclined stratification (radar package 4).

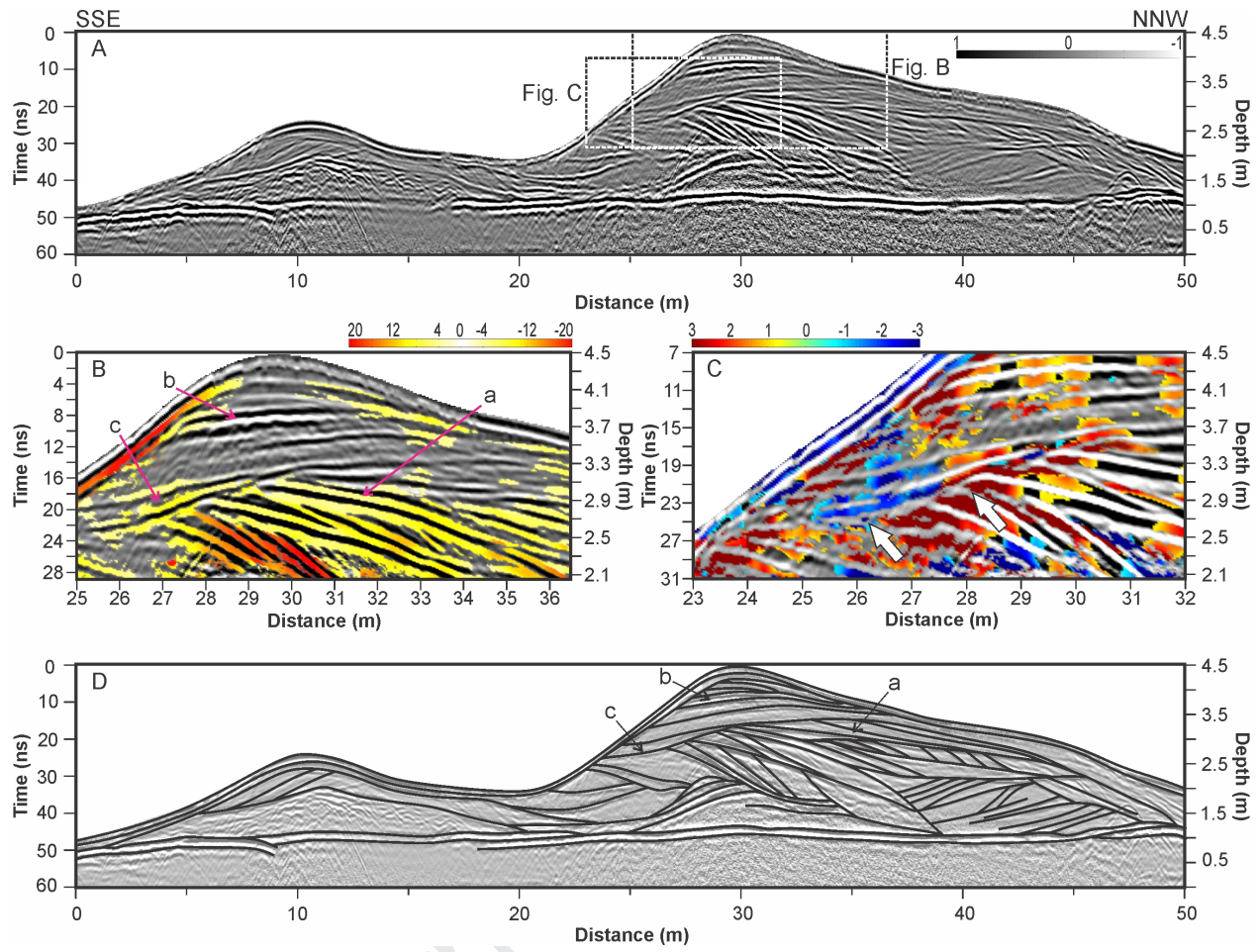
Fig. 11: Schematic sections of fluvial-aeolian interaction deposits note that the muddy bed was used as a key level for correlation. A and B indicate the localization of the sections in figure 1: A corresponds to point 7 and B to point 1.

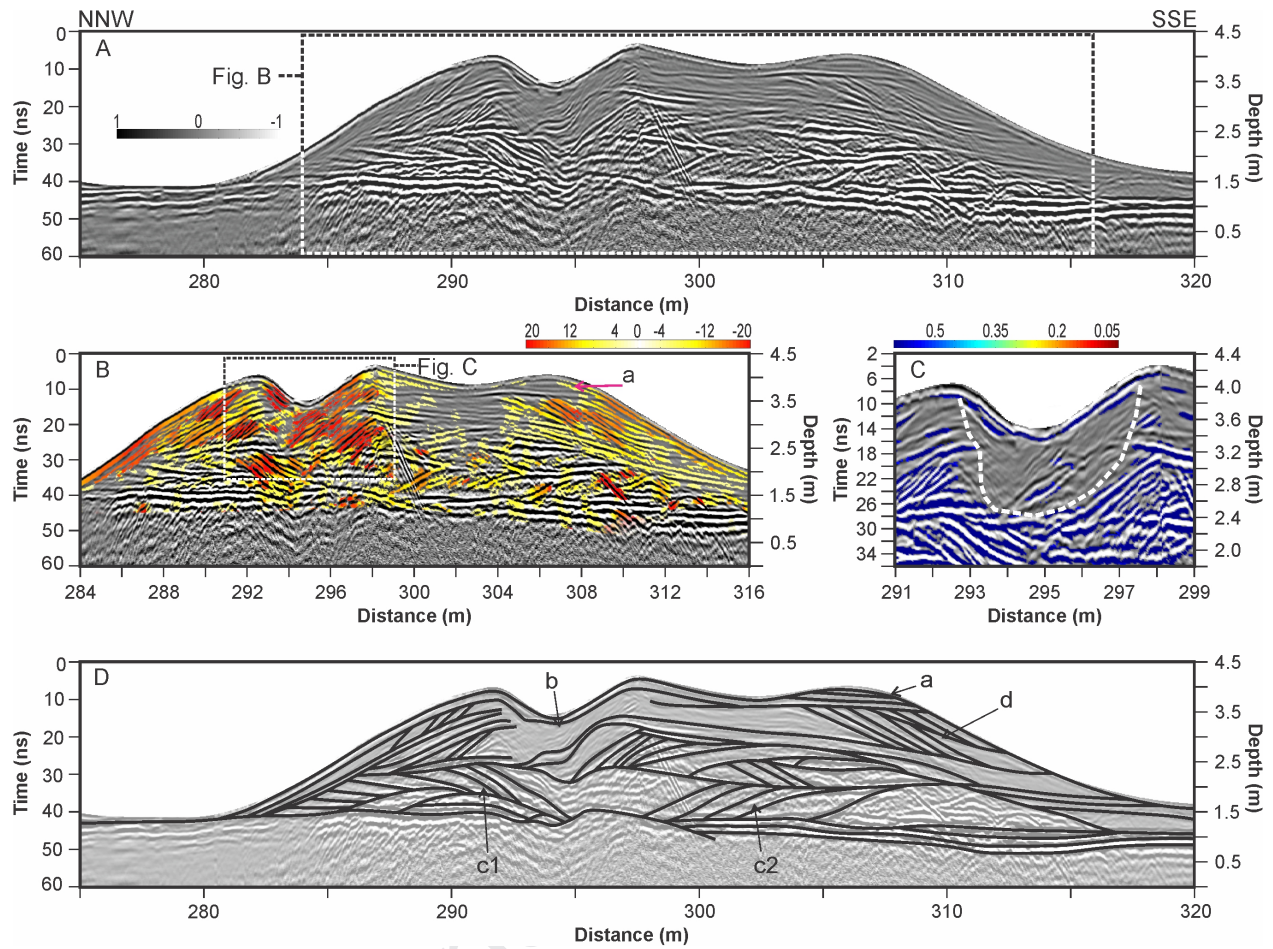
Fig. 12: A. Aeolian cross-bedded set separated by a horizontal truncation surface from the overlying horizontal-laminated sandstones, this situation reproduces the relationship between radar packages 1, 2 or 3 with radar package 4 (see Fig. 10C). B. Lateral view of a trough cross-bedded set corresponding to a small high-sinuosity dune, this type of structure reproduces trough-shaped radar surfaces in GPR sections. C. Fine-grained laminated sandstones corresponding to sandy interdunes.

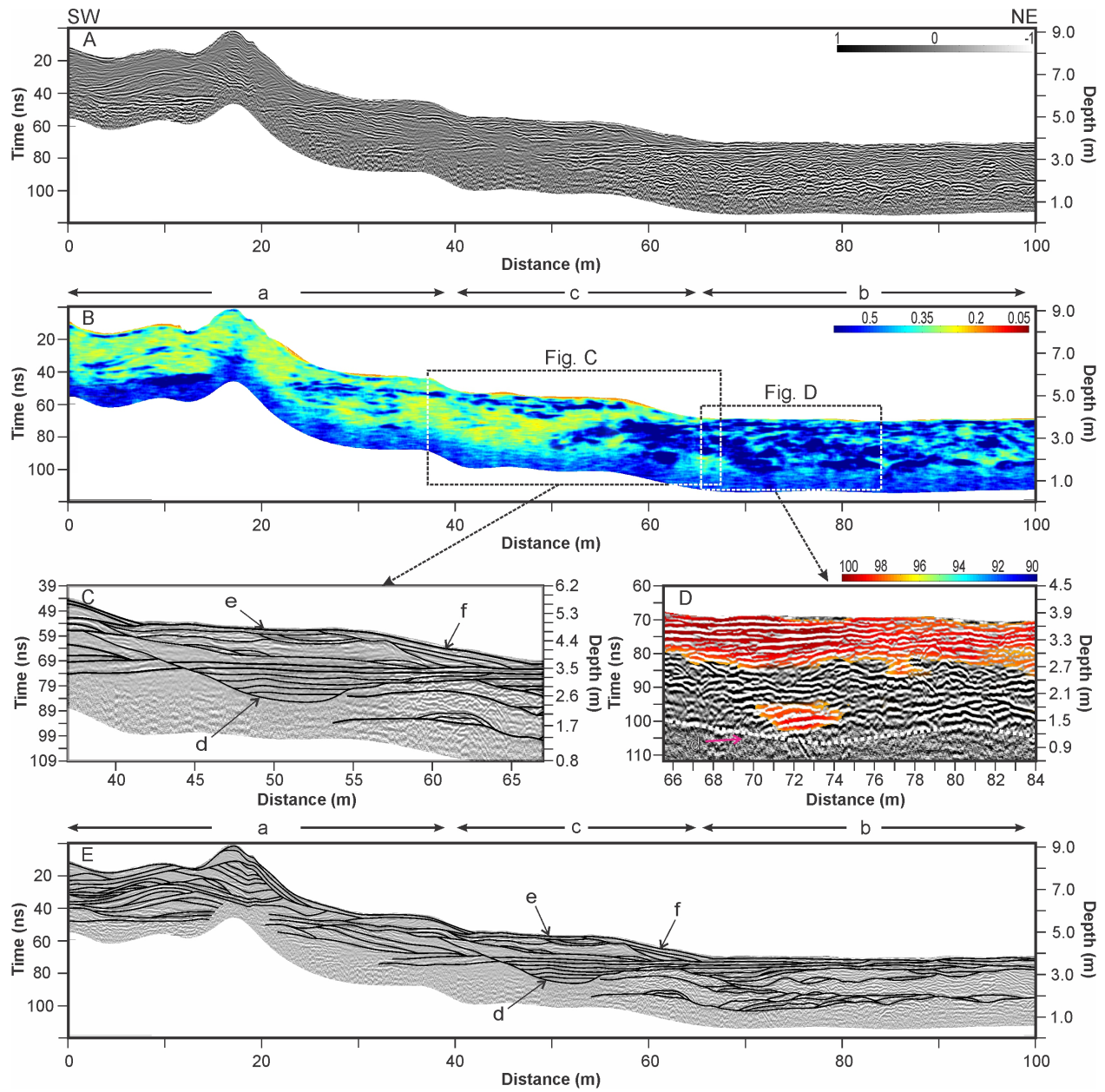
997 **Fig. 13:** Conceptual model establishing the relation between the radar
998 packages and the time evolution of the fluvial-aeolian interaction field of
999 Guandacol.

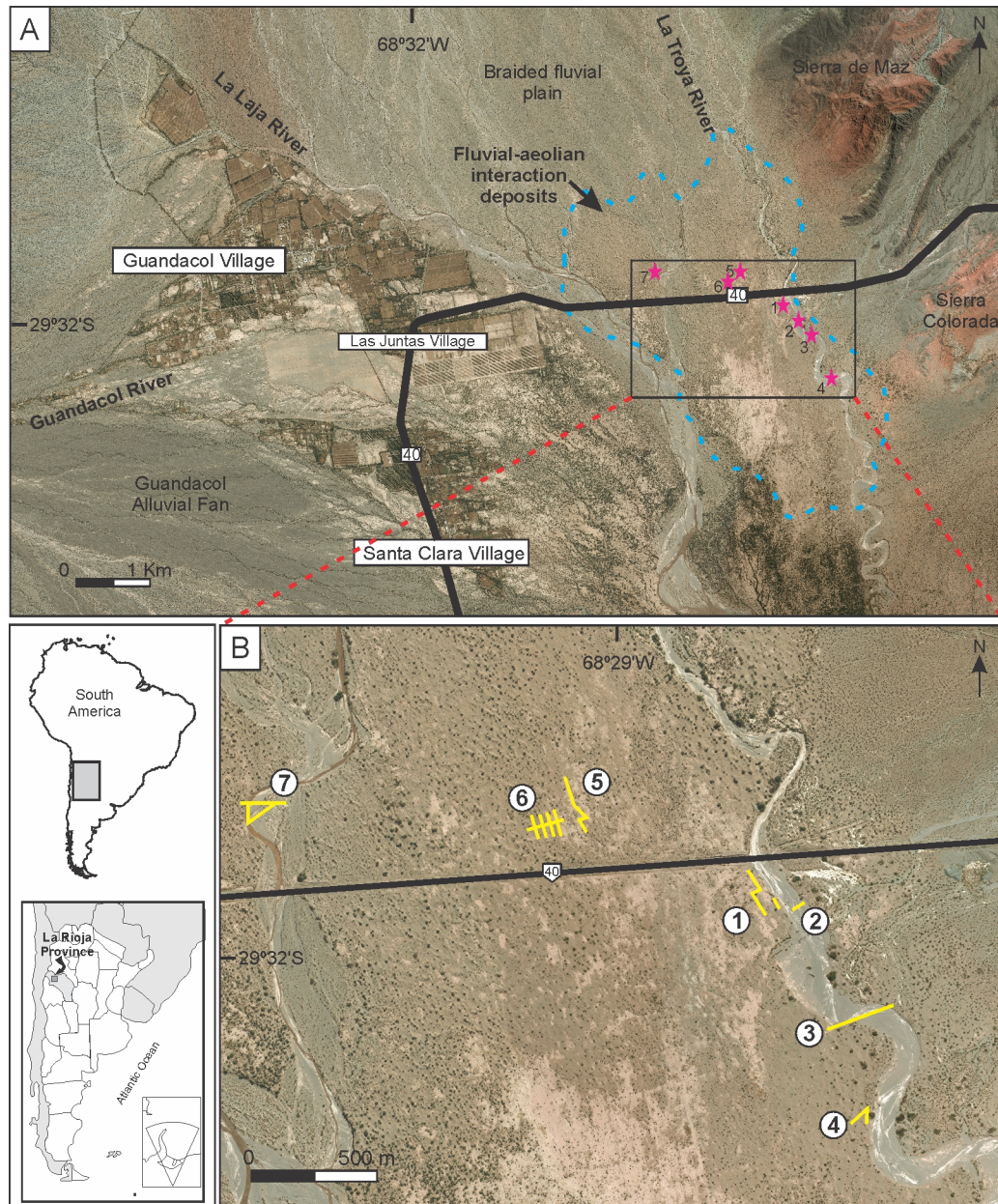
Journal Pre-proof

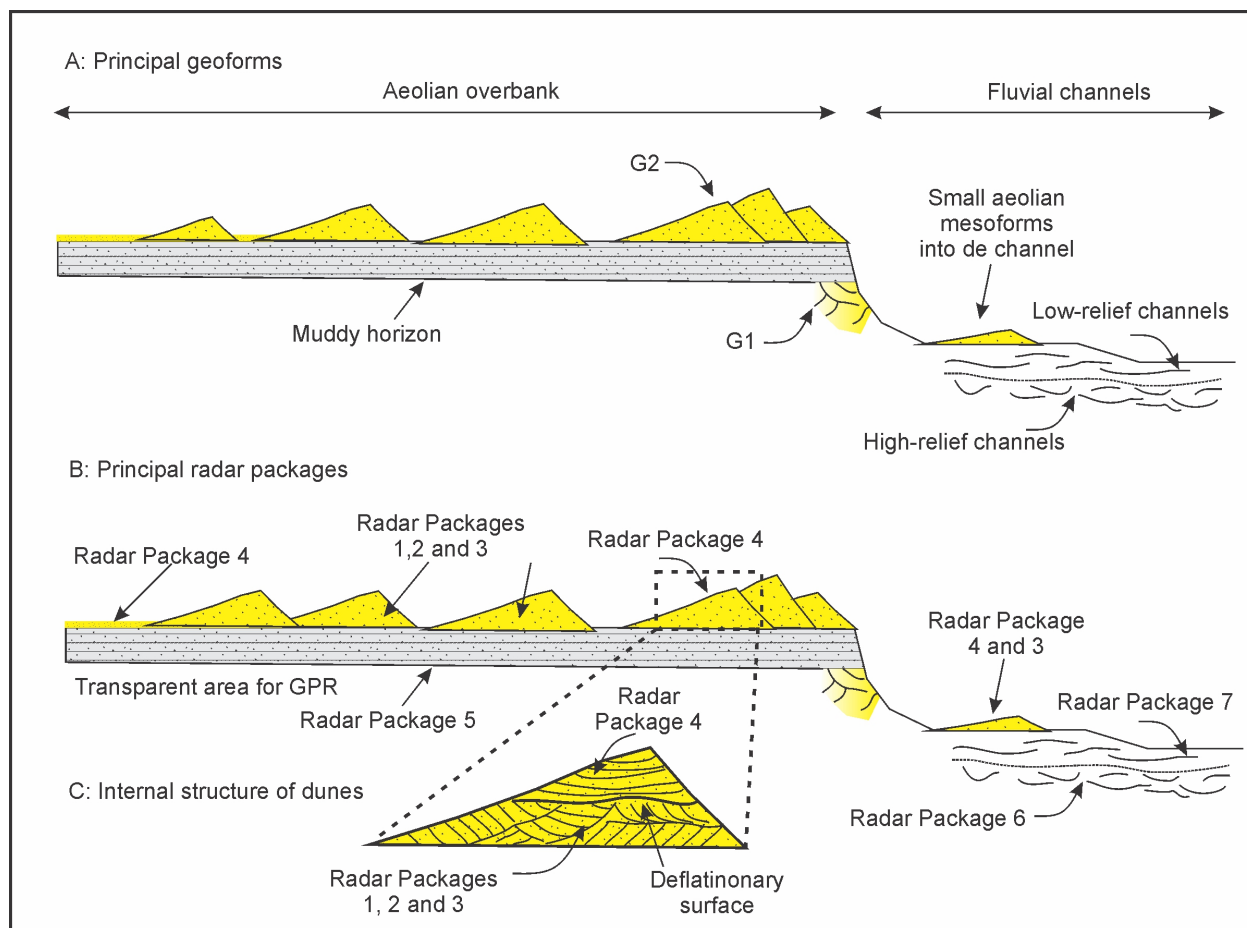


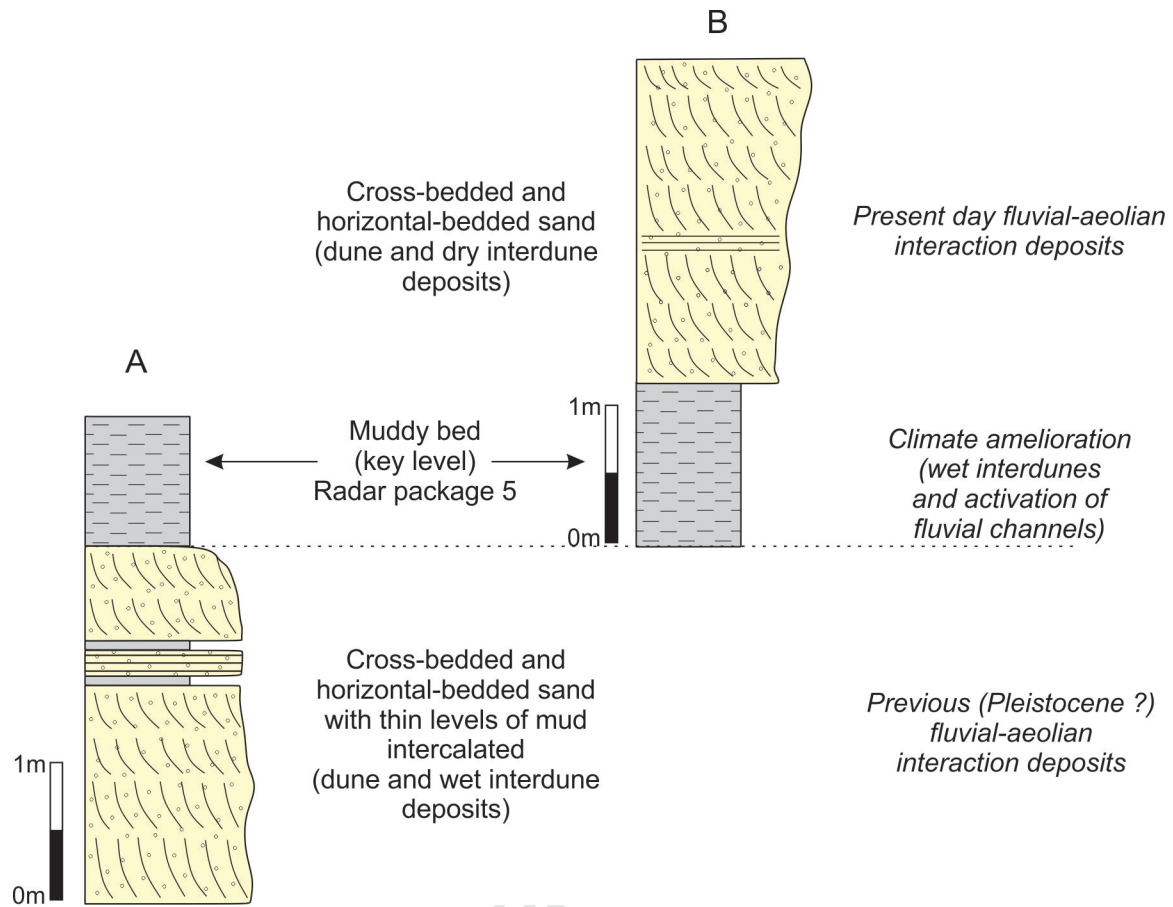


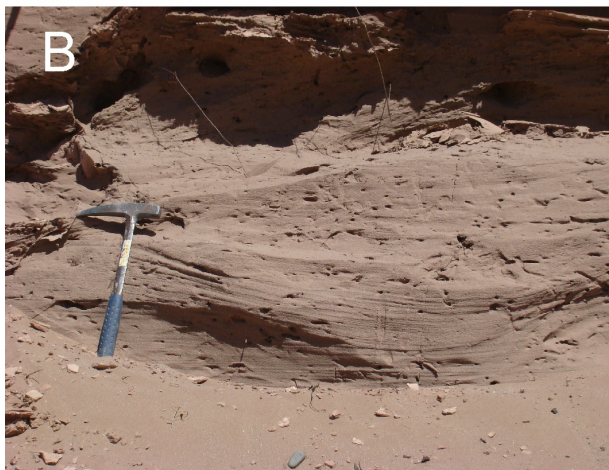


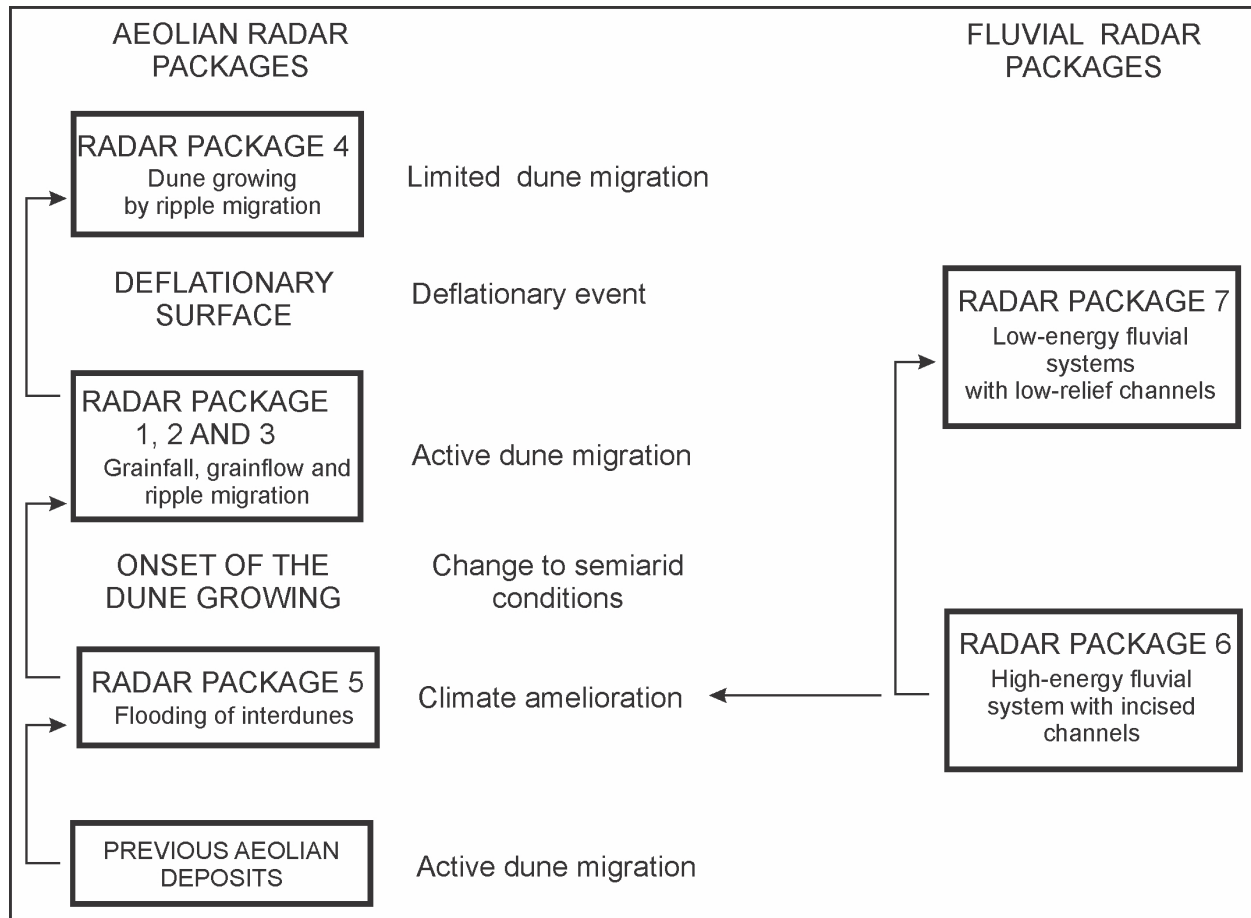




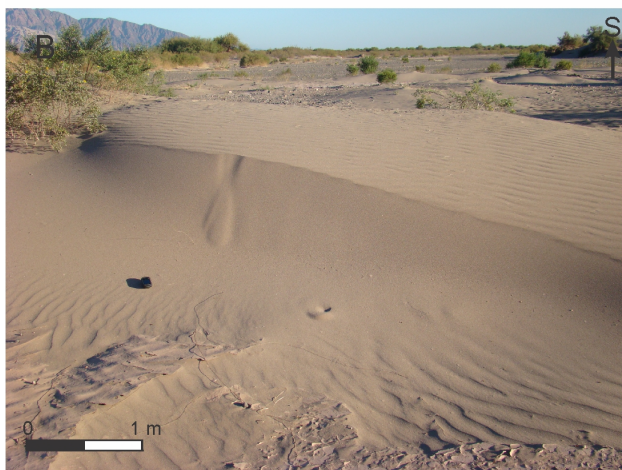




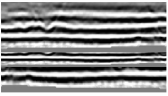




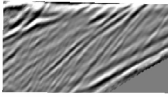




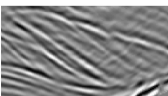
RADAR SURFACES



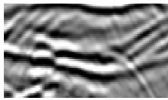
Horizontal
and subhorizontal



Inclined with basal
angular contact



Inclined with basal
tangential contact



Trough-shaped

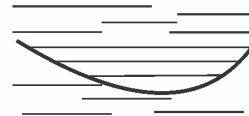
RADAR BOUNDING SURFACES



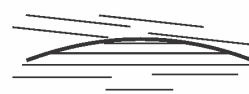
Plane
horizontal



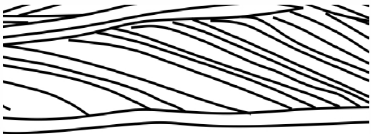


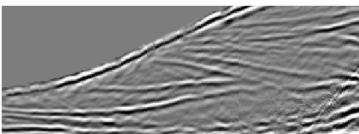

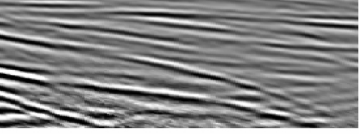

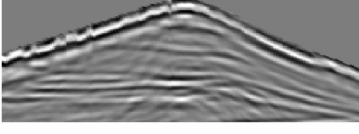



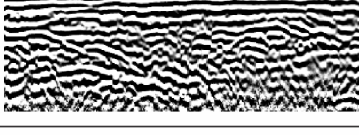
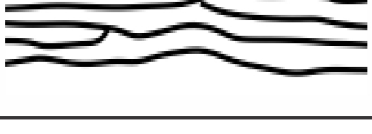
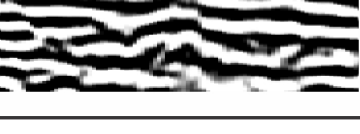
Plane inclined



Concave-up



Convex-up

<p>Radar Package 1</p> 		<p>Migration of low-sinuosity dunes with occasional reactivation surfaces</p>
<p>Radar Package 2</p> 		<p>Migration of high-sinuosity dunes with occasional reactivation surfaces</p>
<p>Radar Package 3</p> 		<p>Migration of mesoforms on dune faces</p>
<p>Radar Package 4</p> 		<p>Sandy interdunes or upper part of dunes dominated by ripple migration</p>
<p>Radar Package 5</p> 		<p>Muddy interdunes</p>
<p>Radar Package 6</p> 		<p>Filling of high-relief fluvial plains including incised channels</p>
<p>Radar Package 7</p> 		<p>Filling of low-relief fluvial plains including shallow channels</p>

GPR images allow identifying internal architecture of dune and fluvial deposits

Attribute analysis make evident and reinforce properties of the reflection patterns

Radar packages offer a conceptual model in the study of fluvial-aeolian environments

Journal Pre-proof

Declaration of interests

☒ The authors declare that they have no known competing financial interests or personal relationships that could have appeared to influence the work reported in this paper.

☐ The authors declare the following financial interests/personal relationships which may be considered as potential competing interests: